

# Enhanced activity for the oxygen reduction reaction in microporous water

Received: 30 August 2022

Accepted: 7 April 2023

Published online: 15 May 2023

 Check for updates

Agnes E. Thorarinsdottir<sup>1,3</sup>, Daniel P. Erdosy<sup>1,3</sup>, Cyrille Costentin<sup>2</sup>✉, Jarad A. Mason<sup>1</sup>✉ & Daniel G. Nocera<sup>1</sup>✉

Electrocatalysis of small gas molecules driven by renewable energy sources offers a promising route to carbon-neutral fuels and chemicals. Such small-molecule conversion reactions rely on water as a source of protons and electrons, however, thus limiting energy and power densities owing to the low solubility of gas molecules in water. The oxygen reduction reaction (ORR) is an exemplar of such limitations. Here we demonstrate that the high O<sub>2</sub>-carrying capacity of aqueous solutions endowed with porosity arising from microporous nanocrystals with hydrophobic internal surfaces and hydrophilic external surfaces—termed microporous water—enhances ORR electrocatalysis in water. Use of silicalite-1 nanocrystals to form an O<sub>2</sub>-concentrating microporous electrolyte solution increases the ORR current so much that the activity of Pt, typically thought to be an ideal ORR catalyst, is partially limiting, thus allowing the intrinsic catalytic ORR activity of Pt to be measured directly.

Catalysis of small gas molecules driven by electricity generated from renewable energy sources offers a promising route to carbon-neutral fuels and chemicals<sup>1–4</sup>. Large-scale implementation of small molecule conversions relies on water as a source of protons and electrons<sup>5–7</sup>. An exemplar energy conversion process involving gases is the H<sub>2</sub>/O<sub>2</sub> ↔ H<sub>2</sub>O fuels cycle<sup>8</sup> where renewable energy may be stored in the chemical bonds of the products of the water-splitting reaction, O<sub>2</sub> and H<sub>2</sub>, and then recovered on demand with the oxygen reduction reaction (ORR), via a hydrogen fuel cell<sup>8</sup>. The low solubilities of O<sub>2</sub> and H<sub>2</sub> in water<sup>9</sup>, and more generally of most other small gas molecules of energy consequence (for example, N<sub>2</sub> and CO<sub>2</sub>), substantially limits the achievable current densities using liquid-phase electrocatalysis. Although gas- or vapour-fed gas diffusion electrodes enable one to two orders of magnitude greater current densities than liquid-phase systems<sup>10–13</sup>, key challenges remain because of the complexity of the two-phase and three-phase interfaces, complex and non-uniform catalyst microenvironments, and electrode flooding, which adversely affect their durability and long-term performance<sup>14–16</sup>. Moreover, the requirements of certain device configurations, such as those of various membrane reactors<sup>17–19</sup>, preclude the possibility of a gas–liquid

interface. This provides an imperative to overcome mass transport limitations imposed by poor gas solubilities.

One strategy to circumvent the low solubility of gases in water is to introduce organic additives such as perfluorocarbons (PFCs). The resulting two-phase aqueous–organic systems provide higher gas solubilities owing to the much higher solubilities of non-polar gases in organic media as compared with aqueous media<sup>20</sup>. Nevertheless, high PFC concentrations of 25 vol.% are necessary to achieve even a modest 1.8× increase in ORR current in alkaline conditions<sup>21</sup>. Beyond lower O<sub>2</sub> capacities, PFCs are very weakly associated, leading to emulsion instability as droplets undergo Ostwald ripening over time, and PFCs are prone to evaporating from the aqueous solution owing to their high vapour pressure. An alternative strategy centres on employing porous solids that remain empty and able to adsorb gas molecules even when uniformly dispersed in a solvent, so-called porous liquids<sup>22–25</sup>. Though most porous liquids contain organic solvents, certain microporous nanocrystals with hydrophobic internal surfaces and hydrophilic external surfaces can form aqueous porous liquids—termed microporous water—that feature much higher gas concentrations than conventional aqueous solutions<sup>26</sup>. The weak physisorptive interactions that lead to

<sup>1</sup>Department of Chemistry and Chemical Biology, Harvard University, Cambridge, MA, USA. <sup>2</sup>Département de Chimie Moléculaire, CNRS, Université Grenoble Alpes, Grenoble, France. <sup>3</sup>These authors contributed equally: Agnes E. Thorarinsdottir, Daniel P. Erdosy.

✉e-mail: [cyrille.costentin@univ-grenoble-alpes.fr](mailto:cyrille.costentin@univ-grenoble-alpes.fr); [mason@chemistry.harvard.edu](mailto:mason@chemistry.harvard.edu); [dnocera@fas.harvard.edu](mailto:dnocera@fas.harvard.edu)

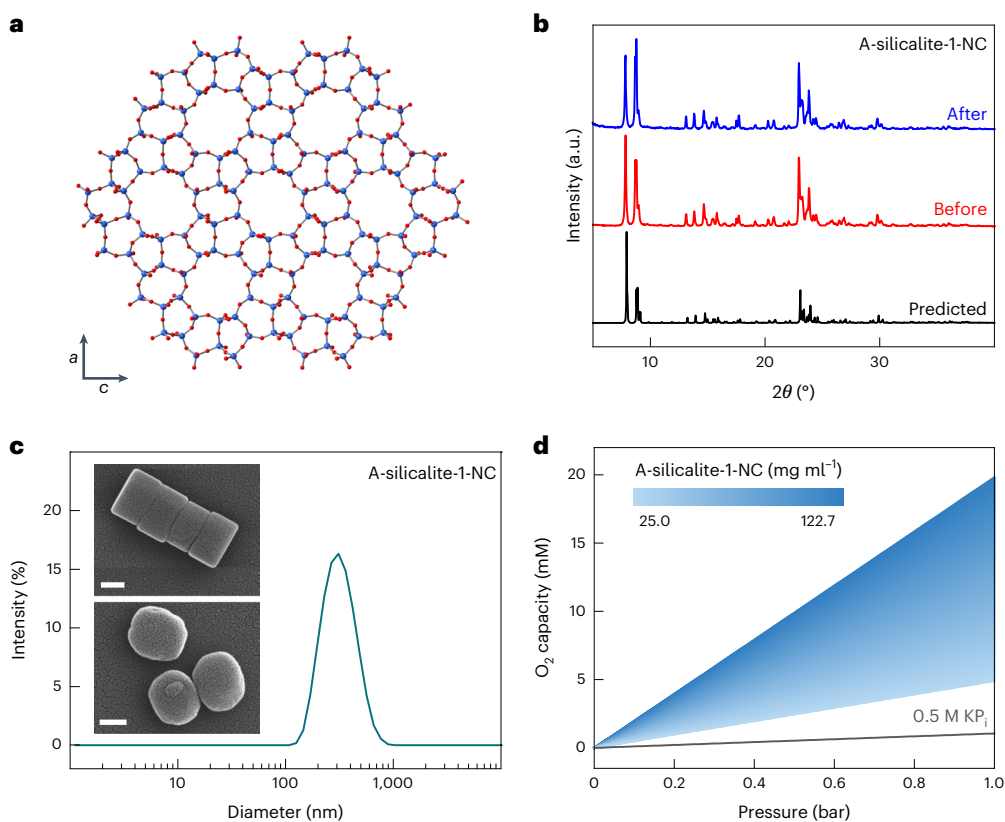


**Fig. 1 | Characterization of A-silicalite-1-NCs in solid state and aqueous solution.** **a**, Part of a crystal structure of silicalite-1-NC viewed along the crystallographic *b* axis; blue and red spheres denote Si and O atoms, respectively. **b**, PXRD data collected for A-silicalite-1-NCs before (red) and after (blue) performing ORR catalysis in phosphate-buffered water (0.5 M in phosphorus) solutions at pH 7.0. Predicted powder pattern derived from the reported crystal structure is shown in black for comparison. **c**, DLS particle size distribution of

A-silicalite-1-NCs in phosphate-buffered water (0.5 M in phosphorus) solution at pH 7.0. Inset: SEM images of A-silicalite-1-NCs before ORR catalysis as viewed top-down (bottom) and side-on (top). Scale bars, 100 nm. **d**, Comparison of O<sub>2</sub> capacities of phosphate-buffered water (0.5 M KP<sub>1</sub>) solutions at pH 7.0 and ambient temperature without (grey) and with 25.0–122.7 mg ml<sup>-1</sup> of A-silicalite-1-NCs (blue), as obtained from O<sub>2</sub> release measurements in deoxygenated water.

the high gas capacities of microporous water also facilitate fast gas exchange kinetics, making these solutions well suited for liquid-phase electrochemical catalysis. The approach of boosting gas concentration through physisorptive interactions provides a path to catalysis at higher operating currents and also could enable the assessment of the intrinsic activity of electrocatalysts over a wide potential range, as mass transport limitations imposed by the diffusion of gaseous substrates to the catalyst surface would be minimized or completely circumvented.

In this Article, we report the ORR activity of a Pt/C electrocatalyst in water endowed with microporosity afforded by the hydrophobic cavities of zeolitic nanocrystals (silicalite-1-NCs). Aqueous dispersions of silicalite-1-NCs adsorb and release O<sub>2</sub> reversibly, carrying up to two orders of magnitude more O<sub>2</sub> than pure water<sup>26</sup>. In the presence of a 6.7 vol.% aqueous solution of these O<sub>2</sub>-concentrating nanocrystals, a 3.8–3.9× increase in the ORR current density is observed for a Pt/C electrocatalyst in acidic and neutral conditions. This increase in current density is such that Pt, typically considered to be a superior ORR catalyst<sup>27</sup>, becomes the partial rate-limiting determinant of ORR in the microporous water, thus reducing the mass transport contribution and allowing the intrinsic catalytic ORR activity of Pt to be easily measured by rotating disk electrode (RDE) voltammetry.

## Results

### Solid- and solution-state properties of silicalite-1-NCs

Silicalite-1 is a pure-silica zeolite with hydrophobic micropores<sup>28</sup> and a mordenite framework inverted structure type<sup>29</sup> with two types

of interconnected channels: sinusoidal and straight channels running along the crystallographic *a* and *b* axis (Fig. 1a), respectively. Silicalite-1-NCs were synthesized by a hydrothermal route using a modification of a reported procedure<sup>30</sup> (A-silicalite-1-NCs; Methods). The crystallinity and phase purity of A-silicalite-1-NCs were verified by powder X-ray diffraction (PXRD) (Fig. 1b), and the morphology was assessed by scanning electron microscopy (SEM). The A-silicalite-1-NCs exhibit a cylindrical morphology (Fig. 1c, inset and Supplementary Fig. 1), as indicated by disk-shaped (average diameter of 197 ± 16 nm; Supplementary Fig. 2 and Supplementary Table 1) and rectangular (height ca. 125 nm) features when viewed from top-down and side-on, respectively. Gas adsorption measurements revealed an O<sub>2</sub> adsorption capacity of 3.8(4) × 10<sup>2</sup> mM bar<sup>-1</sup> at 20 °C for the solid-state material (Supplementary Table 2), which is far higher than the 1.42 mM bar<sup>-1</sup> of O<sub>2</sub> that is dissolved in water at the same temperature (Fig. 1d, grey trace). Owing to their hydrophilic external surfaces that are capped with silanol and silanolate species, A-silicalite-1-NCs may be dispersed in a variety of neutral aqueous solutions (Supplementary Fig. 3), including high-concentration phosphate buffers (Fig. 1c). Although aggregation of A-silicalite-1-NCs does occur over time in aqueous solutions of high ionic strength, such behaviour does not affect the impact of the nanocrystals on ORR catalysis (vide infra). Moreover, O<sub>2</sub> release experiments confirm that the silicalite-1-NCs reversibly adsorb O<sub>2</sub> at a density comparable to that in the solid state, even when surrounded by an aqueous phosphate electrolyte (Fig. 1d, blue shaded region and Supplementary Table 3).

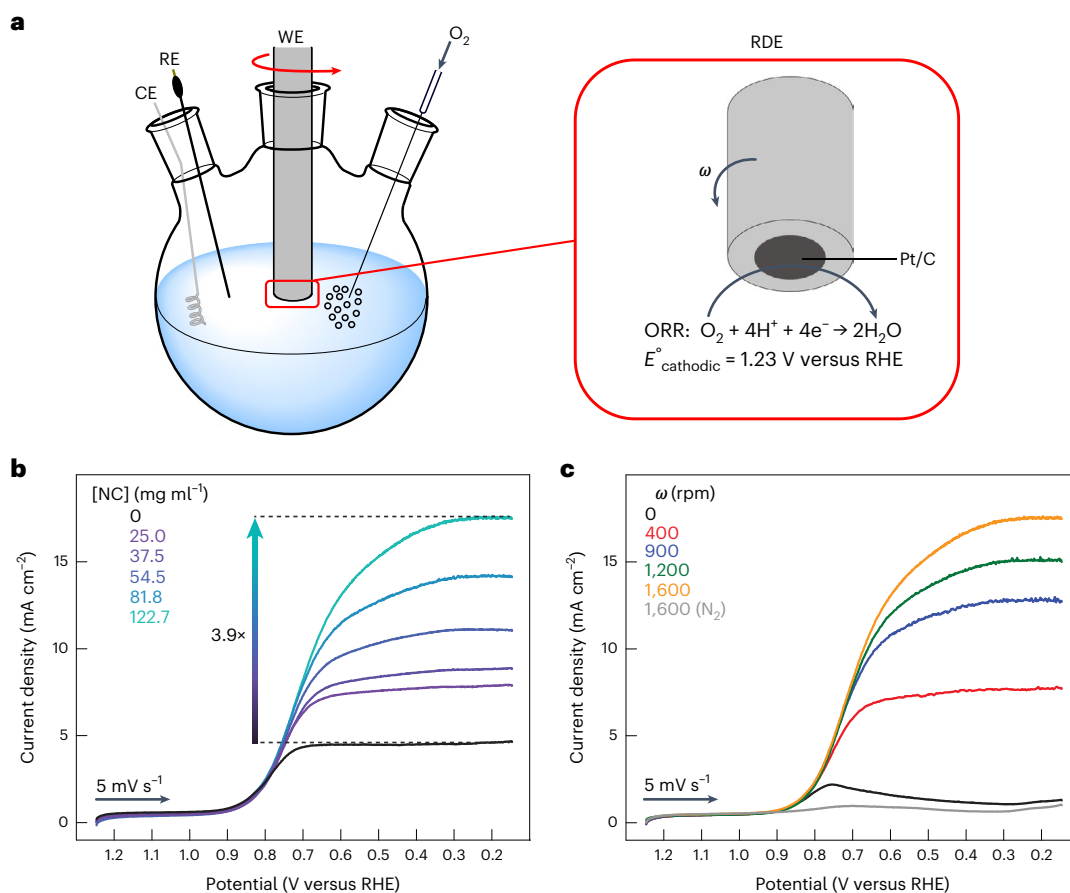


**Fig. 2 | ORR catalysis.** **a**, A schematic highlighting the RDE set-up employed for ORR catalysis experiments using a glassy carbon working electrode (WE) with a Pt/C catalyst film, a leakless Ag/AgCl-based reference electrode (RE) and a Pt-mesh counter electrode (CE). **b**, RDE voltammograms collected in O<sub>2</sub>-saturated phosphate-buffered water (0.5 M KP<sub>i</sub>) solutions at pH 7.0 containing 0–122.7 mg ml<sup>-1</sup> of A-silicalite-1-NCs at a scan rate of 5 mV s<sup>-1</sup> and an electrode rotation rate of 1,600 rpm. **c**, RDE voltammograms collected in

O<sub>2</sub>-saturated phosphate-buffered water (0.5 M KP<sub>i</sub>) solutions at pH 7.0 containing 122.7 mg ml<sup>-1</sup> of A-silicalite-1-NCs at a scan rate of 5 mV s<sup>-1</sup> and electrode rotation rates of 0–1,600 rpm. The voltammogram collected in N<sub>2</sub>-saturated phosphate-buffered water (0.5 M KP<sub>i</sub>) solution at pH 7.0 at an electrode rotation rate of 1,600 rpm is shown in grey for comparison. The reported current density values are normalized by the geometric surface area of the working electrode, and all potentials are reported in V versus RHE.

### Impact of silicalite-1-NCs on ORR electrocatalysis

To examine the effect of microporous on ORR electrocatalysis, we performed RDE voltammetry on aqueous solutions containing varying concentrations of A-silicalite-1-NCs. ORR by RDE voltammetry enables precise control of convective flow for mass transport<sup>31</sup>, where the effects of mass transport and electrode kinetics can be often quantified separately using the Koutecký–Levich equation<sup>32</sup>. A thin film of a commercial carbon-supported platinum catalyst (Pt/C; 60 wt.% Pt) on a glassy carbon RDE was employed as the working electrode (Fig. 2a) to be consistent with previously reported ORR studies<sup>27,33–35</sup>; ORR on Pt/C proceeds exclusively via the four-electron/four-proton reduction pathway<sup>33,34</sup>. A high concentration of phosphate buffer (total phosphorus species of 0.5 M, potassium phosphate, KP<sub>i</sub>) was employed as the electrolyte solution to maintain the local pH at the cathode near that of the bulk solution.

Figure 2b shows the recorded current density traces (RDE rotation rate,  $\omega$  = 1,600 rpm) for ORR in phosphate-buffered water at pH 7.0 (black trace) and for increasing concentrations of A-silicalite-1-NCs from 25.0 to 122.7 mg ml<sup>-1</sup> (Supplementary Table 4). In the absence of A-silicalite-1-NCs, the expected S-shape profile is obtained with a plateau current density of 4.5 mA cm<sup>-2</sup> as a result of O<sub>2</sub> mass transport limitations; this result is typical of ORR on Pt/C in aqueous solutions where a plateau current density of 4–6 mA cm<sup>-2</sup> is observed, with the exact value depending on the nature and concentration of the electrolyte<sup>27,34</sup>.

Conversely, the plateau current density for ORR increases monotonically with increasing concentration of A-silicalite-1-NCs (Supplementary Fig. 4), reaching a value of 17.5 mA cm<sup>-2</sup> for phosphate-buffered water containing 122.7 mg ml<sup>-1</sup> of A-silicalite-1-NCs (Fig. 2b, teal trace). We note that the kinematic viscosity ( $\nu$ ; Methods) of solutions containing A-silicalite-1-NCs is higher than that of pure phosphate-buffered water (Supplementary Table 6), though the contribution of the kinematic viscosity to the limiting ORR current density ( $j_{\text{lim}}$ ) is minimal owing to a  $j_{\text{lim}} \propto \nu^{-1/6}$  dependence<sup>33</sup>.

Figure 2c shows the increase in the ORR current density with  $\omega$  for phosphate-buffered water containing A-silicalite-1-NCs at 122.7 mg ml<sup>-1</sup> ( $\omega$  dependence for other concentrations of A-silicalite-1-NCs is shown in Supplementary Fig. 5). The increase in ORR current density with rotation rate indicates mass transport limitations, but not exclusively as the observation of a plateau is delayed to lower potentials (that is, higher overpotentials) as compared with pure phosphate-buffered water. Importantly, the plateau in ORR current density is shifted by over 0.4 V in microporous water (0.7 V and 0.25 V versus the reversible hydrogen electrode (RHE) in the absence and presence of A-silicalite-1-NCs, respectively), indicating that the activity-dominated current density of the Pt/C catalyst may be extracted in this potential range (vide infra). The observations of a 3.9× increase in ORR current density together with partially rate-limiting catalyst activity for the microporous phosphate electrolyte solutions as compared with pure phosphate-buffered

water indicate that hydrophobic silicalite-1-NCs represent a formidable strategy to increase ORR electrocatalytic performance.

### Influence of particle size and type on ORR performance

We next assessed the impact of silicalite-1 particle size on the ORR catalytic performance. As opposed to the cylindrical and larger particle size of A-silicalite-1-NCs, B-silicalite-1-NCs (Methods for synthesis; Supplementary Fig. 6 for PXRD) are spherical (Supplementary Fig. 7) with an average diameter of  $92 \pm 13$  nm (Supplementary Fig. 8 and Supplementary Table 1). The ORR catalysis at selected concentrations (Supplementary Table 7) was examined using the same procedure as for A-silicalite-1-NCs. The overall ORR behaviour is the same for identical concentrations of the two silicalite-1-NC samples (Supplementary Fig. 9), but slightly lower ORR current densities were observed for the smaller particle size, which probably results from their slightly lower O<sub>2</sub> capacity (Supplementary Table 2).

To investigate the impact of the nature of the zeolite nanocrystals on ORR catalytic performance, ORR catalysis on a Pt/C catalyst in phosphate-buffered water (0.5 M in phosphorus) solutions at pH 7.0 was carried out in the presence of aluminosilicate zeolite L nanocrystals (LTL-NCs; Methods for synthesis; Supplementary Fig. 10 for PXRD). LTL-NCs exhibit asymmetric morphology (Supplementary Fig. 11) and feature hydrophilic pores, which are filled with water molecules when immersed in aqueous solutions. In contrast to silicalite-1-NCs, LTL-NCs (Supplementary Table 10) do not provide enhanced ORR catalytic current densities for a Pt/C catalyst over that recorded in pure phosphate-buffered water (Supplementary Fig. 12). The poor ORR performance of hydrophilic LTL-NCs is attributed to water-filled pores. As all three types of zeolite-NC remain intact after ORR operation, as confirmed by PXRD (Fig. 1b and Supplementary Figs. 6 and 10) and SEM (Supplementary Figs. 1, 2, 7, 8 and 11) analyses, these observations indicate that O<sub>2</sub> carried in the dry pores of silicalite-1-NCs in water is critical for increasing the concentration of O<sub>2</sub> in the vicinity of the catalyst and engendering the observed enhancement in ORR current density. As further evidence of that explanation, no enhancement in ORR current density is observed in the presence of non-calcined A-silicalite-1-NCs (Supplementary Fig. 17), which feature pores filled with organic structure-directing agent (SDA) and thus lead to an O<sub>2</sub> capacity similar to that of pure phosphate-buffered water (Supplementary Table 2).

### ORR performance in acid

To investigate how the electrolyte impacts ORR catalytic performance of the Pt/C electrocatalyst in the presence of silicalite-1-NCs, we repeated the ORR electrocatalysis study in 0.5 M H<sub>2</sub>SO<sub>4</sub> (pH 0.3) solutions containing varying concentrations of A-silicalite-1-NCs from 25.0 to 122.7 mg ml<sup>-1</sup> (Supplementary Table 17). In the presence of 122.7 mg ml<sup>-1</sup> of A-silicalite-1-NCs, the ORR current density is 21.1 mA cm<sup>-2</sup> at 0.25 V versus RHE ( $\omega = 1,600$  rpm), representing a 3.8× increase over that observed in pure 0.5 M H<sub>2</sub>SO<sub>4</sub> solution (Supplementary Figs. 22 and 23). These results are in good agreement with the 3.9× enhancement in ORR current density observed in phosphate-buffered water at pH 7.0, indicating that the presence of silicalite-1-NCs improves ORR catalytic performance so long as the nanocrystals remain stable under the operating conditions of catalysis.

### Catalyst stability and particle effects on ORR performance

The Pt/C electrocatalyst was investigated in both phosphate-buffered water (pH 7.0) and 0.5 M H<sub>2</sub>SO<sub>4</sub> (pH 0.3) solutions to assess whether the catalyst is affected by the presence of silicalite-1-NCs. For each electrolyte solution under O<sub>2</sub> saturation, a three-part RDE ORR experiment was performed using a single Pt/C catalyst film. First, the RDE voltammogram was collected in the absence of silicalite-1-NCs, then the RDE voltammogram was collected in the presence of 118.5 mg ml<sup>-1</sup> of A-silicalite-1-NCs and finally the RDE voltammogram was collected again in the absence of silicalite-1-NCs. As shown in Supplementary

Fig. 26, for both electrolyte solutions, the two RDE voltammograms for collected pre- and post-introduction to a 118.5 mg ml<sup>-1</sup> solution of A-silicalite-1-NCs are identical, indicating that the Pt/C catalyst is not modified in the presence of silicalite-1-NCs.

As suspended particles have been shown to influence mass transport at RDEs under certain conditions arising from perturbation of the diffusion layer thickness<sup>36,37</sup>, we also investigated whether such particle effects are operative under our experimental conditions. The LTL-NCs offer an ideal control for examining whether nanoparticles affect the observed enhancement in ORR current density as they are of similar chemical composition, morphology and size to that of A-silicalite-1-NCs. However, as mentioned above, no enhancement in ORR current density is observed for aqueous solutions of LTL-NCs. As a further control, we performed ORR electrocatalysis measurements on identical, but non-calcined A-silicalite-1-NCs. As presented in Supplementary Table 2, non-calcined A-silicalite-1-NCs display minimal porosity due to pore blockage with the immobilized organic SDAs. As shown in Supplementary Figs. 17 and 25, no enhancement in ORR current density is observed for non-calcined A-silicalite-1-NCs in phosphate-buffered water (0.5 M phosphorus, pH 7.0) and 0.5 M H<sub>2</sub>SO<sub>4</sub> (pH 0.3) solutions, respectively. Finally, following previously reported approaches to define the influence of suspended particles on mass transfer in RDE experiments, we monitored the ferricyanide to ferrocyanide electroreduction. Supplementary Fig. 27 shows the current density traces for the ferricyanide reduction on a glassy carbon working electrode in Ar-saturated phosphate-buffered water (0.5 M phosphorus, pH 7.0) and 0.5 M H<sub>2</sub>SO<sub>4</sub> (pH 0.3) solutions containing varying concentrations of A-silicalite-1-NCs from 25.0 to 122.7 mg ml<sup>-1</sup>. As displayed in Supplementary Fig. 27, A-silicalite-1-NCs have no notable effects on the RDE voltammograms for ferricyanide reduction in both electrolyte solutions, indicating that changes in diffusion layer thickness arising from inert particle effects are negligible under our operating conditions. Collectively, these data illustrate that increased O<sub>2</sub> concentration in the vicinity of the electrocatalyst is the primary reason for the observed enhancement in ORR current density in microporous water as opposed to physical perturbation of the electrical double layer.

### Electrokinetics modelling of ORR catalysis

Insight into the benefit of microporous water on ORR catalysis is obtained from electrokinetics modelling (Supplementary Note 5) of ORR catalysis in the absence (Supplementary Fig. 28) and presence of silicalite-1-NCs. Figure 3a shows an electrokinetics model where the bulk O<sub>2</sub>-saturated aqueous solution is composed of free O<sub>2</sub> molecules with a diffusion coefficient  $D_{O_2}$  in equilibrium with O<sub>2</sub> molecules adsorbed in silicalite-1-NCs (ZO<sub>2</sub>) with an apparent diffusion coefficient  $D_{ZO_2}$ . As the diffusion coefficient of silicalite-1-NCs ( $D_s$ ) is approximately four orders of magnitude smaller than  $D_{O_2}$ , the transport of O<sub>2</sub> by silicalite-1-NCs is best viewed as a hopping-type mechanism of O<sub>2</sub> between nanocrystals in which the equilibrium between O<sub>2</sub> and ZO<sub>2</sub> is fast and such that  $D_{ZO_2}$  is of the same order of magnitude as  $D_{O_2}$  (Supplementary Fig. 29). The reaction scheme and catalytic sequence employed for the modelling are highlighted in Fig. 3b,c, respectively. We note that our model assumes that O<sub>2</sub> molecules adsorbed in silicalite-1-NCs cannot be directly reduced; rather, O<sub>2</sub> needs to desorb before reduction, thus giving rise to a CE (chemical step preceding an electrochemical step) type mechanism. The redox characteristics of native catalyst active sites are obtained from fitting the voltammetric features of the Pt/C catalyst film in the absence of O<sub>2</sub> (Supplementary Fig. 28). This leads to a non-ideal Nernstian behaviour akin to a distribution of standard potentials and blocking of surface sites, which can be rationalized by the polycrystalline nature of Pt/C particles and the possible role of phosphate<sup>38,39</sup> and sulfate<sup>40-42</sup> electrolytes in the redox properties of individual crystal faces of Pt.

The model in Fig. 3 furnishes an excellent fit of the experimental data, as shown in Fig. 3d and Supplementary Fig. 30 for studies in



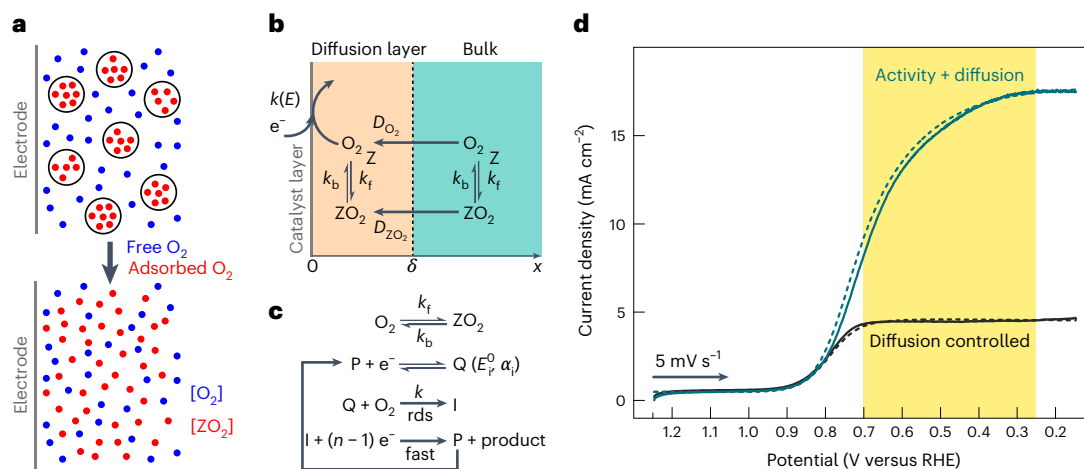


**Fig. 3 | Electrokinetics modelling of ORR catalysis.** **a**, Schematic diagram highlighting the foundation of our electrokinetics model for ORR catalysis in the presence of silicalite-1-NCs (here denoted as Z), where the bulk solution is composed of free  $\text{O}_2$  molecules (blue spheres) in equilibrium with  $\text{O}_2$  molecules adsorbed in silicalite-1-NCs (red spheres). **b**, Reaction scheme used for electrokinetics modelling. Note that  $\text{O}_2$  molecules adsorbed in silicalite-1-NCs ( $\text{ZO}_2$ ) cannot be directly reduced at the electrode surface, thus leading to a CE-type mechanism.  $\delta$ , size of the diffusion layer set by  $\omega$ ;  $x$ , distance from electrode surface. **c**, Summary of the catalytic sequence employed for electrokinetics modelling. P and Q correspond to the oxidized and reduced forms of the active catalyst sites, respectively, I is an intermediate,  $n$  is the

stoichiometric number (here  $n = 4$ ),  $E_i^0$  is the standard reduction potential for the P/Q couple,  $\alpha_i$  is the charge transfer coefficient,  $k_f$ ,  $k_b$  and  $k$  are rate constants and rds denotes the rate-determining step. **d**, RDE voltammograms collected in  $\text{O}_2$ -saturated phosphate-buffered water (0.5 M KP<sub>i</sub>) solutions at pH 7.0 containing 0 mg ml<sup>-1</sup> (black) and 122.7 mg ml<sup>-1</sup> (teal) of A-silicalite-1-NCs at a scan rate of 5 mV s<sup>-1</sup> and an electrode rotation rate of 1,600 rpm. The dashed lines correspond to fits to the experimental data (solid lines) using the electrokinetics model highlighted in **a–c** and detailed in Supplementary Note 5. The yellow shaded region highlights the expansion of the potential regime in which the activity-dominated current density may be extracted, as achieved in the presence of A-silicalite-1-NCs.

phosphate-buffered water (0.5 M in phosphorus, pH 7.0) solutions and in Supplementary Fig. 31 for studies in 0.5 M  $\text{H}_2\text{SO}_4$  (pH 0.3) solutions. Parameters used in the model are summarized in Supplementary Tables 20 and 21 (phosphate-buffered water) and Supplementary Tables 22 and 23 (0.5 M  $\text{H}_2\text{SO}_4$ ). The model predicts maximum kinetic current densities (that is, in the absence of  $\text{O}_2$  mass transport limitations) of 27.4 mA cm<sup>-2</sup> and 37.6 mA cm<sup>-2</sup> in phosphate-buffered water (pH 7.0) and 0.5 M  $\text{H}_2\text{SO}_4$  (pH 0.3) solutions, respectively, (Supplementary Fig. 32) whereas the measured ORR plateau current densities in the absence of silicalite-1-NCs are only 4.5 mA cm<sup>-2</sup> and 5.6 mA cm<sup>-2</sup> in phosphate-buffered water (pH 7.0) and 0.5 M  $\text{H}_2\text{SO}_4$  (pH 0.3) solutions, respectively. This disparity between calculated and observed current densities highlights the dramatic limitation that  $\text{O}_2$  mass transport imposes on the ORR in aqueous media. As shown in Fig. 2b and Supplementary Fig. 22, by employing a solution containing 122.7 mg ml<sup>-1</sup> (corresponding to 6.7 vol.%) of A-silicalite-1-NCs, we observe plateau current densities of 17.5 mA cm<sup>-2</sup> and 21.4 mA cm<sup>-2</sup> in phosphate-buffered water (pH 7.0) and 0.5 M  $\text{H}_2\text{SO}_4$  (pH 0.3) solutions, respectively, and thus, are able to approach the calculated achievable current densities. The benefit of employing microporous water for ORR electrocatalysis is further highlighted schematically in Supplementary Fig. 33, in which non-porous and microporous aqueous electrolyte solutions are compared. Moreover, our strategy enables us to observe the intrinsic catalytic activity of the Pt/C ORR electrocatalyst over a wide potential range. Whereas the apparent catalytic rate constants obtained from the electrokinetics modelling of  $k_{\text{app}} = 2.25 \times 10^2 \text{ M}^{-1} \text{ s}^{-1}$  in phosphate-buffered water (pH 7.0) and  $k_{\text{app}} = 3.0 \times 10^2 \text{ M}^{-1} \text{ s}^{-1}$  in 0.5 M  $\text{H}_2\text{SO}_4$  (pH 0.3) do not limit ORR in pure electrolyte solutions at applied potentials >0.25 V versus RHE, the enhancement afforded by microporous water is manifested in the curvature of the current density traces extending from 0.7 V to 0.25 V versus RHE (Fig. 3d, yellow shaded region, and Supplementary Fig. 22e). The ability to perform electrocatalysis in such an expanded mixed kinetic- and diffusion-controlled current regime allows a direct experimental measure of the intrinsic

activity of the catalyst, which should be useful as a tool for the design of ORR electrocatalysts.

## Conclusions

The foregoing results demonstrate the ability of aqueous solutions endowed with microporosity arising from microporous nanocrystals with hydrophobic internal surfaces and hydrophilic external surfaces—termed microporous water—to improve the ORR catalytic performance of a Pt/C electrocatalyst through increased supply of  $\text{O}_2$ . A modest concentration of zeolite (6.7 vol.%) results in an increase in ORR current by 3.8–3.9 $\times$  in acidic and neutral electrolyte solutions, exceeding previously examined additives such as concentrated PFC emulsions (1.8 $\times$  increase in ORR current with 25 vol.% PFC emulsions<sup>21</sup>). Accordingly, our work highlights an unexplored area in electrocatalysis centred on the employment of microporous water to achieve highly concentrated solutions of gases at the electrode where catalysis may occur at enhanced current densities owing to reduced mass transport limitations. This provides a platform for accessing intrinsic catalytic properties across a wide range of potentials.

## Methods

### Materials

Sixty (60) wt.% platinum on high surface area Ketjenblack EC-300J was used as received from Fuel Cell Store. Anhydrous potassium hydrogen phosphate (98+%) and potassium dihydrogen phosphate (99+%) were used as received from Strem Chemicals. Aluminium hydroxide ( $\text{Al}(\text{OH})_3$ ) was used as received from Beantown Chemicals. Tetrapropylammonium hydroxide (TPAOH, ca. 20 wt.% in water) was used as received from TCI. Potassium hexacyanoferrate(II) trihydrate (ACS reagent grade, 98.5–102.0%), anhydrous potassium hexacyanoferrate(III) (99.98% trace metals basis), tetraethyl orthosilicate (TEOS, 98%), potassium hydroxide (KOH, ACS reagent grade,  $\geq 85\%$ ), LUDOX HS-40 colloidal silica (40 wt.%  $\text{SiO}_2$  in water), HPLC grade ethanol (EtOH) and Nafion perfluorinated resin solution (5 wt.% in a mixture of lower aliphatic alcohols

and water) were used as received from Sigma Aldrich. Sulfuric acid (TraceMetal Grade) was used as received from Fisher Scientific. Nitrogen gas (99.99%), argon gas (99.99%) and ultrahigh-purity oxygen gas (99.994%) were used as received from Airgas. All electrolyte solutions were prepared with type I water (EMD Millipore, 18.2 MΩ cm resistivity).

### Synthesis of A-silicalite-1-NCs

Silicalite-1-NCs exhibiting a cylindrical shape with an average diameter of ca. 200 nm and an average height of ca. 125 nm were synthesized following a procedure adapted from a previous report<sup>30</sup>. In a representative synthesis, aqueous TPAOH (39.17 ml, 22.3 wt.%), type I water (44.52 ml) and TEOS (26.31 ml) were combined in a 250 ml glass bottle. The initially biphasic mixture was stirred for 23 h at 500 rpm, allowing the TEOS to become hydrolysed in the alkaline environment and liberate EtOH into the solution. Following hydrolysis, the molar ratio of this solution was 9.1 TPAOH:25 SiO<sub>2</sub>:880 H<sub>2</sub>O:100 EtOH. The homogeneous solution was loaded into a 200 ml Parr acid digestion vessel, and the vessel was sealed and heated to 170 °C for 29 h in an oven. After allowing the vessel to cool, the as-synthesized A-silicalite-1-NCs were collected and washed five times with type I water in 50 ml centrifuge tubes. Note that 10 min of centrifugation at 7,830 rpm (7,197 relative centrifugal force, r.c.f.) was sufficient to precipitate the majority of the product. After the final wash, the product was dried in a centrifuge tube at 70 °C. The dried product was collected and finely ground into a powder. This powder was subsequently placed in an enamelled crucible and loaded into a tube furnace. The powder was heated in air from room temperature to 550 °C over 2 h and then held at 550 °C for 10 h. After calcination, A-silicalite-1-NCs were allowed to cool and then collected.

### Synthesis of B-silicalite-1-NCs

Silicalite-1-NCs exhibiting a spherical shape with an average diameter of ca. 90 nm were synthesized following a procedure adapted from a previous report<sup>43</sup>. In a representative synthesis, TPAOH (48.88 ml, 22.3 wt.%), type I water (13.29 ml) and TEOS (32.83 ml) were combined in a 250 ml glass bottle. The initially biphasic mixture was stirred for 24 h at 500 rpm, allowing the TEOS to become hydrolysed in the alkaline environment and liberate EtOH into the solution. Following hydrolysis, the molar ratio of this solution was 9.1 TPAOH:25 SiO<sub>2</sub>:480 H<sub>2</sub>O:100 EtOH. The homogeneous solution was loaded into a 200 ml Parr acid digestion vessel, and the vessel was sealed and heated to 90 °C for 48 h in an oven. After allowing the vessels to cool, the as-synthesized B-silicalite-1-NCs were collected and washed six times with type I water in 50 ml centrifuge tubes. After the final wash, the product was dried in a centrifuge tube at 70 °C. The dried product was collected and finely ground into a powder. This powder was subsequently placed in an enamelled crucible and loaded into a tube furnace. The powder was heated in air from room temperature to 550 °C over 30 min and then held at 550 °C for 10 h. After calcination, B-silicalite-1-NCs were allowed to cool and then collected.

### Synthesis of LTL-NCs

In a representative synthesis adapted and modified from a previous report<sup>44</sup>, KOH (14.12 g, 0.252 mol) and Al(OH)<sub>3</sub> (2.43 g, 0.0312 mol) were added to type I water (45 ml) in a 100 ml glass jar containing a Teflon-coated stir bar. The resulting solution was heated in an oil bath to 105 °C for about 3 h to allow the Al(OH)<sub>3</sub> to dissolve in the alkaline solution. Afterwards, the solution was allowed to cool for 50 min, and subsequently 28.60 ml of 40 wt.% LUDOX (14.87 g SiO<sub>2</sub>, 0.248 mol SiO<sub>2</sub>) was added. The resulting mixture was sonicated briefly before being stirred at room temperature for 20.5 h. Note that, over time, the mixture visibly homogenized and completely fluidized. Afterwards, the solution was cooled and loaded into Parr acid digestion vessels. The vessels were sealed and heated to 180 °C in an oven. After allowing the vessels to cool, the as-synthesized LTL-NCs were collected and diluted with type I water and precipitated via centrifugation at 7,830 rpm (7,197 r.c.f.).

The supernatant was then removed, and fresh type I water was added to the centrifuge tubes. The centrifugation process was repeated for a total of 15 cycles to give a crude aqueous solution of LTL-NCs.

### Synthesis of non-calcined A-silicalite-1-NCs

The synthetic procedure was adapted from the same report used to make calcined A-silicalite-1-NCs<sup>30</sup>. In a representative synthesis, aqueous TPAOH (33.27 ml, 22.7 wt.%), type I water (39.74 ml) and TEOS (22.99 ml) were combined in a 250 ml glass bottle. The initially biphasic mixture was stirred for 24 h at 500 rpm, allowing the TEOS to become hydrolysed in the alkaline environment and liberate EtOH into the solution. Following hydrolysis, the molar ratio of this solution was 9.1 TPAOH:25 SiO<sub>2</sub>:880 H<sub>2</sub>O:100 EtOH. The homogeneous solution was loaded into a 200 ml Parr acid digestion vessel, and the vessel was sealed and heated to 170 °C for 31 h in an oven. After allowing the vessel to cool, the as-synthesized A-silicalite-1-NCs were collected and washed extensively with type I water to remove excess SDA. Note that the SDA is partitioned between the interior and exterior of the nanocrystals; the former cannot be removed by simple washing with water as the pore apertures are too narrow to permit SDA migration. Thus, washing with water was aimed at removing all accessible SDA and uncrystallized SiO<sub>2</sub> from the reaction solution. Washing was assumed to be complete when no further change was observed in the residual organic content of the sample, assessed as follows. After seven washes with type I water in 50 ml centrifuge tubes, an aliquot was taken and dried for thermogravimetric analysis to quantify the residual non-SiO<sub>2</sub> content, which was found to be 13%. The sample was subsequently washed five more times, and a new aliquot was taken for thermogravimetric analysis. Since the residual non-SiO<sub>2</sub> content of this sample remained about the same, the sample was assumed to be fully washed, and the remaining non-SiO<sub>2</sub> content was assumed to be mostly SDA that was trapped inside the pores of the zeolite. Upon completion of the washing step, the sample was recombined into a single tube and diluted with sufficient type I water to obtain a fluid solution with relatively low viscosity that was used directly for analysis.

### Formation of aqueous solutions of activated silicalite-1-NCs

To create a solution of activated A-silicalite-1-NCs, a calcined powder consisting of A-silicalite-1-NCs was added to type I water and sonicated in an ultrasonic bath at 40 kHz frequency for 40 h. To purify and remove large aggregates suspended in solution, the aqueous dispersion was centrifuged at 1,500 rpm (264 r.c.f.) for 15 min. After transferring the supernatant to a new centrifuge tube, the dispersion was then centrifuged three more times at 1,500 rpm for 5 min each, and the supernatant was decanted into a new tube each time. After the last centrifugation cycle, A-silicalite-1-NCs were washed once by centrifuging at 7,830 rpm (7,197 r.c.f.) for 15 min, the supernatant was discarded and the precipitated A-silicalite-1-NCs were redispersed in fresh type I water. The preparation of aqueous solutions of activated B-silicalite-1-NCs was performed in a similar manner as the procedure detailed for A-silicalite-1-NCs, with slight modifications to the duration of sonication and specific purification steps.

### Formation of aqueous solutions of LTL-NCs

After completion of 15 washes, the crude LTL-NCs were dispersed in 35 ml of type I water. To purify and remove large aggregates, this solution was subjected to size selection by centrifugation at 7,830 rpm (7,197 r.c.f.) for variable time periods ranging between 1 and 5 min, with the resulting precipitate inspected for visible white aggregates. The supernatant was decanted into a fresh tube each time, and the size selection process was continued until very little white precipitate was observed.

### Catalyst film preparation

A catalyst ink was prepared by mixing 5 mg of 60 wt.% platinum on high surface area Ketjenblack EC-300J with 990 μl of EtOH and 10 μl

of Nafion perfluorinated resin solution (5 wt.% in a mixture of lower aliphatic alcohols and water). The ink was sonicated for at least 30 min to provide a homogeneous dispersion, and 10  $\mu\text{l}$  of this dispersion was dropcasted onto a 5 mm diameter (0.196  $\text{cm}^2$  geometric surface area) glassy carbon RDE (Pine Research). Before use, the glassy carbon electrode was polished using 0.3  $\mu\text{m}$  Alpha alumina powder (CH Instruments) and rinsed with a copious amount of type I water and EtOH, then subsequently dried in air. Note that the resulting black film contained approximately 0.03 mg of platinum. The film was dried in air and wetted with a minimum amount of type I water before being immersed in the sample solution. The average thickness of the catalyst film was estimated to be on the order of a few micrometres ( $<5 \mu\text{m}$ ) using a Tyler Hobson Coherence Correlation Interferometry high-resolution three-dimensional non-contact optical profiler.

### General characterization methods

pH measurements were carried out using a Thermo Scientific Orion 9107APMD double-junction pH electrode with automatic temperature compensation, connected to a VWR sympHony SP70P pH meter. The pH electrode was calibrated using standardized pH buffer solutions at 4.01, 7.00 and 10.01 (Thermo Scientific Orion).

PXRD data were collected at ambient temperature on a D2 Phaser Bruker AXS diffractometer with  $\text{CuK}_\alpha$  radiation ( $\lambda = 1.5418 \text{ \AA}$ ). Each sample was dried and placed onto a low-background Si wafer for measurement. The PXRD data collected for zeolite nanocrystals (zeolite-NCs) before and after performing ORR catalysis are provided in Fig. 1b and Supplementary Fig. 18 (A-silicalite-1-NCs), Supplementary Fig. 6 (B-silicalite-1-NCs), Supplementary Fig. 10 (LTL-NCs) and Supplementary Figs. 13 and 24 (non-calcined A-silicalite-1-NCs).

Brunauer–Emmett–Teller (BET) analysis was used to determine surface areas for the zeolite-NCs from  $\text{N}_2$  adsorption isotherms collected at 77 K. For 77 K  $\text{N}_2$  surface area measurements, gas adsorption for solid samples was measured at a minimum of 50 different pressures between 0 and 0.9 bar, with at least 45 points collected below 0.1 bar (Supplementary Note 1).

### Nanocrystal size analysis

Field emission SEM and dynamic light scattering (DLS) were used to quantify the size distribution of the synthesized nanocrystals. SEM analysis of zeolite-NCs was performed using a Zeiss Ultra Plus instrument. The SEM was operated at an electron beam voltage of 20 kV at a working distance of 5.0 mm, and an in-lens secondary electron detector was used for imaging. In a representative measurement, Si wafers sample holders were washed by sonicating with acetone and isopropanol before being loaded into a plasma cleaner. To prepare samples for imaging, aqueous zeolite-NC solutions were diluted with EtOH, and this ethanolic solution was dropcasted onto the Si substrate. All samples were sputter coated with a 5 nm or 10 nm layer of 80:20 Pt:Pd. To calculate the size distributions of calcined and non-calcined A-silicalite-1-NCs and B-silicalite-1-NCs, SEM images were analysed using ImageJ. Each size distribution was computed using at least 100 individual silicalite-1-NCs. Note that the reported size of a single silicalite-1-NC was defined and calculated as the equivalent diameter of a circle having the same area as each silicalite-1-NC. For A-silicalite-1-NCs, the size was defined in the top-down direction. No notable size changes were observed after ORR catalysis in both 0.5 M potassium phosphate ( $\text{KP}_i$ ) and 0.5 M  $\text{H}_2\text{SO}_4$  solutions, regardless of whether the silicalite-1-NCs were calcined or not. In all cases, the mean diameter was within one standard deviation between samples measured before and after ORR catalysis. These data are presented graphically in Supplementary Figs. 2 and 20 (calcined A-silicalite-1-NCs), Supplementary Fig. 8 (B-silicalite-1-NCs) and Supplementary Fig. 15 (non-calcined A-silicalite-1-NCs), and summarized in Supplementary Tables 1 and 16.

DLS analysis was used to determine the size distributions of silicalite-1-NCs in aqueous solutions. DLS measurements were

performed using a Malvern Panalytical Zetasizer Ultra instrument. To prepare samples for measurements, aqueous silicalite-1-NC solutions were diluted with type I water, 0.5–1.0 M  $\text{KP}_i$  buffer (pH 7.0) or 0.5–1.0 M  $\text{H}_2\text{SO}_4$  to give a final concentration of ca. 1  $\text{mg ml}^{-1}$  of silicalite-1-NCs in type I water with and without 0.5 M  $\text{KP}_i$  buffer (pH 7.0) or 0.5 M  $\text{H}_2\text{SO}_4$  electrolyte. Note that dilution is required to obtain accurate DLS data. Samples were sonicated or vortexed for at least 10 s right before data acquisition. The reported data are an average of five to six individual measurements on a representative silicalite-1-NC sample, where each measurement is an average of at least five runs. The data are reported as intensity distribution in lieu of number distribution owing to the non-applicability of certain criteria needed to transform the former into the latter. Mie theory, used to convert intensity distribution to number distribution<sup>45</sup>, is accurate only when the solution is homogeneous and spherically symmetric, and both the real and imaginary components of the refractive index of the solution must be known. The obtained particle size distribution curves for calcined A-silicalite-1-NCs in aqueous solutions are shown in Fig. 1c and Supplementary Figs. 3 and 21, and the analogous size distribution curves obtained for non-calcined A-silicalite-1-NCs are provided in Supplementary Fig. 16. The particle size distribution curves for B-silicalite-1-NCs in neutral aqueous solutions are given in Supplementary Fig. 3. We note that A-silicalite-1-NCs do undergo aggregation over time in aqueous solutions of high ionic strength, and this is especially pronounced in strongly acidic electrolyte solutions (for example, 0.5 M  $\text{H}_2\text{SO}_4$ ); however, such aggregation does not affect the impact of A-silicalite-1-NCs on ORR catalysis with Pt/C electrocatalyst in aqueous solutions (vide supra).

### Solid-state gas adsorption measurements

Gas adsorption measurements were carried out on solid zeolite-NCs at 77 K for  $\text{N}_2$  and at 20  $^\circ\text{C}$  for  $\text{O}_2$ . Samples for measurements were activated before measurement by heating to 175  $^\circ\text{C}$  and evacuating using a Smart VacPrep gas adsorption sample preparation device (Micromeritics Instrument) equipped with a turbomolecular pump. Sample analysis was performed using a Micromeritics MicroActive 3Flex 3500 adsorption analyser. To maintain a constant temperature during measurements and minimize fluctuations during  $\text{O}_2$  isotherm measurements, the sample analysis tubes were immersed in a large, jacketed water bath that was held at 20  $^\circ\text{C}$  (temperature error of approximately  $\pm 0.4 \text{ }^\circ\text{C}$ ).  $\text{O}_2$  isotherms were collected by measuring gas adsorption at 20 different pressures in roughly 0.05 bar increments between 0 and 1 bar. The  $\text{O}_2$  Henry's constants of solid zeolite-NCs were obtained from the slope of the linear fit applied to the obtained data (Supplementary Table 2).

### Bulk oxygen concentration measurements

Measurements of the bulk concentration of dissolved  $\text{O}_2$  were carried out concurrently with electrochemical analysis using a PyroScience GmbH FireSting-PRO optical  $\text{O}_2$  meter equipped with a temperature sensor for automatic temperature compensation. A self-adhesive  $\text{O}_2$  sensor spot was attached to the interior and exterior of the glass vessel used as a sample holder for electrochemical measurements. The sensor was calibrated against freshwater conditions using a two-point calibration employing the factory calibration value for 0%  $\text{O}_2$  and the measured value of air-saturated type I water as the two calibration points. The readouts from the  $\text{O}_2$  sensor were used to estimate when saturation conditions under specific gas environments were reached. Note that the readouts from the  $\text{O}_2$  sensor were corrected to account for the salinity of the 0.5 M  $\text{KP}_i$  buffer (pH 7.0) solution (conversion factor of 0.710; Supplementary Note 2). During all electrochemical measurements in  $\text{N}_2$ -saturated buffer solutions, the bulk concentration of dissolved  $\text{O}_2$  was lower than 50  $\mu\text{M}$ . During all electrochemical measurements in  $\text{O}_2$ -saturated buffer solutions, the bulk concentration of dissolved  $\text{O}_2$  was 1.0(1) mM (Supplementary Note 2). Note that the dissolved  $\text{O}_2$  content could not be monitored in situ during electrochemical analysis in 0.5 M  $\text{H}_2\text{SO}_4$  solutions due to incompatibility of



the sensor with strongly acidic environments; thus, identical gas purge times as in 0.5 M  $\text{KPi}$  buffer solutions were used.

### Oxygen capacity of aqueous zeolite-NC solutions

The experimental  $\text{O}_2$  capacity of A-silicalite-1-NC electrolyte solutions was determined from  $\text{O}_2$  release measurements in deoxygenated type I water using a Clark electrochemical  $\text{O}_2$  sensor (Unisense MicroRespiration  $\text{O}_2$  microsensors). The details of the measurements and associated calculations are provided in Supplementary Note 3.

### Viscosity measurements

Dynamic viscosity measurements of 0.5 M  $\text{KPi}$  buffer and 0.5 M  $\text{H}_2\text{SO}_4$  sample solutions with and without zeolite-NCs were conducted at 20 °C using a Kyoto Electronics Manufacturing electromagnetically spinning sphere viscometer (model EMS-1000S) equipped with a temperature-controlled sample holder<sup>46</sup>. Samples were loaded into a glass sample tube equipped with an aluminium ball probe of either 2.0 mm (0.5 M  $\text{KPi}$  and 0.5 M  $\text{H}_2\text{SO}_4$  sample solutions with and without calcined or non-calcined A-silicalite-1-NCs or B-silicalite-1-NCs) or 4.7 mm diameter (0.5 M  $\text{KPi}$  and 0.5 M  $\text{H}_2\text{SO}_4$  sample solutions with and without LTL-NCs), and enough sample was added such that the height of the sample in the tube was at least three times the diameter of the ball used (a requisite condition of the physical model employed by the viscometer). Specifically, at least 400  $\mu\text{l}$  and 800  $\mu\text{l}$  of sample were used when the 2.0 mm and 4.7 mm aluminium balls were employed, respectively. The aluminium ball was rotated at a rate of 500–1,000 Hz, and its movement was traced with a red laser. The viscosity of each sample was determined by the reduction in the rotation rate of the aluminium ball. Measurements using the 2.0 mm and 4.7 mm aluminium balls were conducted with measuring times of 1 s and 5 s, respectively. All measurements on zeolite-NC samples were conducted after ultrasonication at 37 kHz for 30 min or vigorous vortexing for at least 10 s. To ensure that temperature equilibration was achieved, the reported data are an average of at least five individual measurements recorded after leaving the sample in the viscometer for at least 10 min. The dynamic viscosity data obtained for sample solutions of A-silicalite-1-NCs, B-silicalite-1-NCs, LTL-NCs and non-calcined A-silicalite-1-NCs are provided in Supplementary Tables 5 and 18, 8, 11 and 14, respectively. Note that the dynamic viscosity values for non-calcined A-silicalite-1-NCs in 0.5 M  $\text{KPi}$  and 0.5 M  $\text{H}_2\text{SO}_4$  solutions and calcined A-silicalite-1-NCs in 0.5 M  $\text{H}_2\text{SO}_4$  solutions increased over time, probably due to settling of the particles; thus, the reported values may be an underestimation of the dynamic viscosity of the sample solutions during ORR catalysis.

Kinematic viscosity values (in  $\text{mm}^2 \text{s}^{-1}$ ) of the sample solutions were obtained from the measured dynamic viscosity values (in mPa·s) by dividing the dynamic viscosity values by the density of the sample solutions. The error bars for the kinematic viscosity values were determined by error propagation. Note that density values for the zeolite-NC sample solutions were calculated using Supplementary equation (24) (silicalite-1-NCs) and Supplementary equation (25) (LTL-NCs), as described in Supplementary Note 4. The density of 0.5 M  $\text{KPi}$  buffer (pH 7.0) and 0.5 M  $\text{H}_2\text{SO}_4$  (pH 0.3) solutions in the absence of zeolite-NCs was measured to be 1.050  $\text{g ml}^{-1}$  (1,050  $\text{g l}^{-1}$ ) and 1.010  $\text{g ml}^{-1}$  (1,010  $\text{g l}^{-1}$ ), respectively. Supplementary Tables 4 and 17 (A-silicalite-1-NCs), 7 (B-silicalite-1-NCs), 10 (LTL-NCs) and 13 (non-calcined A-silicalite-1-NCs) list the calculated zeolite-NC sample solution densities. The kinematic viscosity data are provided in Supplementary Tables 6 and 19, 9, 12 and 15 for A-silicalite-1-NCs, B-silicalite-1-NCs, LTL-NCs and non-calcined A-silicalite-1-NCs, respectively.

### General descriptions of electrochemical procedures

Electrochemical experiments were conducted in a three-electrode electrochemical cell (working, reference and counter electrodes) at ambient temperature on a CH Instruments potentiostat/galvanostat (model 760D) using a leak-free Ag/AgCl-based reference electrode

(LF-1 from Warner Instruments) and a counter electrode composed of a platinum mesh (99.9%, 52 mesh woven from 0.1-mm-diameter wire, Alfa Aesar) attached to a platinum wire (99.95%, 0.5 mm diameter, Alfa Aesar). Before use, platinum counter electrodes were cleaned by soaking in concentrated nitric acid (TraceSELECT, Fisher Scientific) followed by drying with a butane flame. The leak-free Ag/AgCl-based reference electrode was calibrated using the redox potential of potassium ferri/ferrocyanide in 0.5 M  $\text{KPi}$  buffer solution at pH 7.0 (ref. 47).

Electrode potentials ( $E$ ) were converted to the RHE scale using the following relation:

$$E_{\text{RHE}} = E_{\text{Ag/AgCl}} + 0.238 \text{ V} + RT \ln 10 / F \times \text{pH} \quad (1)$$

where  $E_{\text{RHE}}$  is the converted potential versus RHE,  $E_{\text{Ag/AgCl}}$  is the experimentally measured potential versus a leak-free Ag/AgCl-based reference electrode, 0.238 V is the conversion factor to convert from the Ag/AgCl electrode scale to the normal hydrogen electrode scale, as determined through calibration to the ferri/ferrocyanide redox couple<sup>47</sup>,  $R$  is the gas constant,  $T$  is temperature and  $F$  is the Faraday constant. Note that a solution temperature of 21 °C (294.15 K) and a pH value of 7.0 (0.5 M  $\text{KPi}$ ) or 0.3 (0.5 M  $\text{H}_2\text{SO}_4$ ) were employed for determining  $E_{\text{RHE}}$  for all experiments. Negative currents correspond to anodic reactions (oxidation) and positive currents correspond to cathodic reactions (reduction).

### RDE voltammetry

RDE voltammetry experiments were carried out for samples with and without zeolite-NCs at variable electrode rotation rates (0, 400, 900, 1,200 and 1,600 rpm) in 0.5 M  $\text{KPi}$  buffer (pH 7.0) or 0.5 M  $\text{H}_2\text{SO}_4$  (pH 0.3) solutions under both  $\text{N}_2$  and  $\text{O}_2$  saturation conditions. Specifically, each sample solution was first saturated with  $\text{N}_2$  gas (bulk concentration of dissolved  $\text{O}_2$  below 50  $\mu\text{M}$ ) and the working electrode was pre-conditioned by scanning anodically from the open circuit potential in the potential range of  $-0.05 \text{ V}$  to 1.45 V versus RHE (0.5 M  $\text{KPi}$ , pH 7.0) or  $-0.04 \text{ V}$  to 1.36 V versus RHE (0.5 M  $\text{H}_2\text{SO}_4$ , pH 0.3) at a scan rate of 50  $\text{mV s}^{-1}$  and an electrode rotation rate of 0 rpm for ten cycles. Then, a single cyclic voltammetry scan was collected in the potential range of 0.15 V to 1.25 V versus RHE by scanning anodically from 0.95 V versus RHE at a scan rate of 5  $\text{mV s}^{-1}$  and an electrode rotation rate of 1,600 rpm. Afterwards, the sample solution was saturated with  $\text{O}_2$  gas (bulk concentration of dissolved  $\text{O}_2$  of 1.0(1) mM and 1.3(1) mM in 0.5 M  $\text{KPi}$  buffer and 0.5 M  $\text{H}_2\text{SO}_4$  solutions, respectively). Note that the working electrode was not immersed in the sample solution during the gas saturation processes but kept wetted with type I water to avoid delamination. Single cyclic voltammetry scans were collected for the  $\text{O}_2$ -saturated sample solutions in the potential range of 0.15 V to 1.25 V versus RHE by scanning anodically from 0.95 V versus RHE at a scan rate of 5  $\text{mV s}^{-1}$  and variable electrode rotation rates of 0 rpm to 1,600 rpm. To investigate the influence of suspended silicalite-1-NCs on the mass transfer at an RDE, the reduction of  $\text{K}_3[\text{Fe}(\text{CN})_6]$  was analysed in 0.5 M  $\text{KPi}$  buffer or 0.5 M  $\text{H}_2\text{SO}_4$  solutions containing varying amounts of A-silicalite-1-NCs under Ar saturation conditions using a glassy carbon working electrode. These data are provided in Supplementary Fig. 27. All RDE voltammetry experiments were conducted with a continuous gas flow into the sample solution at a rate of  $1.7(2) \times 10^2 \text{ ml min}^{-1}$ , controlled using a mass flow controller (MKS Technology). Uncompensated solution resistance ( $R_u$ ) was determined to be 1.5–3.7  $\Omega$  (0.5 M  $\text{KPi}$ , pH 7.0) and 0.2–0.9  $\Omega$  (0.5 M  $\text{H}_2\text{SO}_4$ , pH 0.3) using the potential step method (50 mV amplitude) around the open circuit potential. Note, however, that all potentials are reported without applying  $iR_u$  compensation and any background correction. A baseline correction was applied to aid in the comparison of RDE voltammetry data collected for 0.5 M  $\text{KPi}$  buffer (pH 7.0) solutions in the absence and presence of non-calcined A-silicalite-1-NCs. Specifically, the data collected in the presence of non-calcined A-silicalite-1-NCs were adjusted so that the



current density at 1.1 V versus RHE was equivalent for all three datasets displayed in Supplementary Fig. 17c. All current densities are reported on the basis of the geometric electrode surface area (0.196 cm<sup>2</sup>). Independently prepared samples of each type were measured to ensure reproducibility. The provided data are representative examples.

### Electrokinetics modelling

RDE voltammograms collected for samples with and without A-silicalite-1-NCs at variable electrode rotation rates in 0.5 M K<sub>2</sub>P<sub>2</sub>O<sub>7</sub> buffer (pH 7.0) and 0.5 M H<sub>2</sub>SO<sub>4</sub> (pH 0.3) solutions under N<sub>2</sub> and O<sub>2</sub> saturation conditions were simulated using analytical equations derived according to the reaction scheme and catalytic sequence displayed in Fig. 3b,c. The details of electrokinetics modelling and associated equations are provided in Supplementary Note 5.

### Data availability

Details of BET surface area analysis of zeolite-NCs, O<sub>2</sub> solubility in electrolyte solutions, O<sub>2</sub> capacity in zeolite-NC solutions, density of zeolite-NC solutions and electrokinetics modelling along with additional physical and electrochemical characterization data are included in Supplementary Information. Other data are available from the corresponding authors upon reasonable request.

### References

- Nocera, D. G. Proton-coupled electron transfer: the engine of energy conversion and storage. *J. Am. Chem. Soc.* **144**, 1069–1081 (2022).
- Stančin, H., Mikulčić, H., Wang, X. & Duić, N. A review on alternative fuels in future energy system. *Renew. Sustain. Energy Rev.* **128**, 109927 (2020).
- Weber, R. S. Effective use of renewable electricity for making renewable fuels and chemicals. *ACS Catal.* **9**, 946–950 (2019).
- Nocera, D. G. Solar fuels and solar chemicals industry. *Acc. Chem. Res.* **50**, 616–619 (2017).
- Lewis, N. S. & Nocera, D. G. Powering the planet: chemical challenges in solar energy utilization. *Proc. Natl Acad. Sci. USA* **103**, 15729–15735 (2006).
- Cook, T. R. et al. Solar energy supply and storage for the legacy and nonlegacy worlds. *Chem. Rev.* **110**, 6474–6502 (2010).
- Spitler, M. T. et al. Practical challenges in the development of photoelectrochemical solar fuels production. *Sustain. Energy Fuels* **4**, 985–995 (2020).
- Staffell, I. et al. The role of hydrogen and fuel cells in the global energy system. *Energy Environ. Sci.* **12**, 463–491 (2019).
- Battino, R., Seybold, P. G. & Campanell, F. C. Correlations involving the solubility of gases in water at 298.15 K and 101325 Pa. *J. Chem. Eng. Data* **56**, 727–732 (2011).
- Higgins, D., Hahn, C., Xiang, C., Jaramillo, T. F. & Weber, A. Z. Gas-diffusion electrodes for carbon dioxide reduction: a new paradigm. *ACS Energy Lett.* **4**, 317–324 (2019).
- Rabiee, H., Ge, L., Zhang, X., Hu, S., Li, M. & Yuan, Z. Gas diffusion electrodes (GDEs) for electrochemical reduction of carbon dioxide, carbon monoxide, and dinitrogen to value-added products: a review. *Energy Environ. Sci.* **14**, 1959–2008 (2021).
- Lees, E. W., Mowbray, B. A. W., Parlange, F. G. L. & Berlinguette, C. P. Gas diffusion electrodes and membranes for CO<sub>2</sub> reduction electrolyzers. *Nat. Rev. Mater.* **7**, 55–64 (2022).
- Wakerley, D. et al. Gas diffusion electrodes, reactor designs and key metrics of low-temperature CO<sub>2</sub> electrolyzers. *Nat. Energy* **7**, 130–143 (2022).
- Nesbitt, N. T. et al. Liquid–solid boundaries dominate activity of CO<sub>2</sub> reduction on gas-diffusion electrodes. *ACS Catal.* **10**, 14093–14106 (2020).
- Yang, K., Kas, R., Smith, W. A. & Burdyny, T. Role of the carbon-based gas diffusion layer on flooding in a gas diffusion electrode cell for electrochemical CO<sub>2</sub> reduction. *ACS Energy Lett.* **6**, 33–40 (2021).
- Tan, Y. C. et al. Pitfalls and protocols: evaluating catalysts for CO<sub>2</sub> reduction in electrolyzers based on gas diffusion electrodes. *ACS Energy Lett.* **7**, 2012–2023 (2022).
- Hone, C. A. & Kappe, C. O. Membrane microreactors for the on-demand generation, separation, and reaction of gases. *Chem. Eur. J.* **26**, 13108–13117 (2020).
- Luo, T., Abdu, S. & Wessling, M. Selectivity of ion exchange membranes: a review. *J. Membr. Sci.* **555**, 429–454 (2018).
- Oener, S. Z., Foster, M. J. & Boettcher, S. W. Accelerating water dissociation in bipolar membranes and for electrocatalysis. *Science* **369**, 1099–1103 (2020).
- Sato, T., Hamada, Y., Sumikawa, M., Araki, S. & Yamamoto, H. Solubility of oxygen in organic solvents and calculations of the Hansen solubility parameters of oxygen. *Ind. Eng. Chem. Res.* **53**, 19331–19337 (2014).
- Kronberger, H., Bruckner, K. & Fabjan, C. Reduction of oxygen from electrolyte emulsions with high oxygen contents. *J. Power Sources* **86**, 562–567 (2000).
- O'Reilly, N., Giri, N. & James, S. L. Porous liquids. *Chem. Eur. J.* **13**, 3020–3025 (2007).
- Giri, N. et al. Liquids with permanent porosity. *Nature* **527**, 216–220 (2015).
- Fulvio, P. F. & Dai, S. Porous liquids: the next frontier. *Chem* **6**, 3263–3287 (2020).
- Bavykina, A., Cadiau, A. & Gascon, J. Porous liquids based on porous cages, metal organic frameworks and metal organic polyhedra. *Coord. Chem. Rev.* **386**, 85–95 (2019).
- Erdosy, D. P. et al. Microporous water with high gas solubilities. *Nature* **608**, 712–718 (2022).
- Wang, X. et al. Review of metal catalysts for oxygen reduction reaction: from nanoscale engineering to atomic design. *Chem* **5**, 1486–1511 (2019).
- Flanigen, E. M. et al. Silicalite, a new hydrophobic crystalline silica molecular sieve. *Nature* **271**, 512–516 (1978).
- Díaz, I., Kokkoli, E., Terasaki, O. & Tsapatsis, M. Surface structure of zeolite (MFI) crystals. *Chem. Mater.* **16**, 5226–5232 (2004).
- Butt, T. & Tosheva, L. Synthesis of colloidal silicalite-1 at high temperatures. *Microporous Mesoporous Mater.* **187**, 71–76 (2014).
- Lazaridis, T., Stühmeier, B. M., Gasteiger, H. A. & El-Sayed, H. A. Capabilities and limitations of rotating disk electrodes versus membrane electrode assemblies in the investigation of electrocatalysts. *Nat. Catal.* **5**, 363–373 (2022).
- Bard, A. J. & Faulkner, L. R. *Electrochemical Methods: Fundamentals and Applications* (Wiley, 2000).
- Zhong, G. et al. Effect of experimental operations on the limiting current density of oxygen reduction reaction evaluated by rotating-disk electrode. *ChemElectroChem* **7**, 1107–1114 (2020).
- Paulus, U. A., Schmidt, T. J., Gasteiger, H. A. & Behm, R. J. Oxygen reduction on a high-surface area Pt/Vulcan carbon catalyst: a thin-film rotating ring-disc electrode study. *J. Electroanal. Chem.* **495**, 134–145 (2001).
- You, B. et al. Bimetal–organic framework self-adjusted synthesis of support-free nonprecious electrocatalysts for efficient oxygen reduction. *ACS Catal.* **5**, 7068–7076 (2015).
- Caprani, A., De Ficquelmont-Loizos, M. M., Tamisier, L. & Peronneau, P. Mass transfer in laminar flow at a rotating disc electrode in suspensions of inert particles. *J. Electrochem. Soc.* **135**, 635–642 (1988).
- Sonneveld, P. J., Visscher, W. & Barendrecht, E. The influence of suspended particles on the mass transfer at a rotating disc electrode. Non-conducting particles. *J. Appl. Electrochem.* **20**, 563–574 (1990).

38. He, Q. et al. Influence of phosphate anion adsorption on the kinetics of oxygen electroreduction on low index Pt(*hkl*) single crystals. *Phys. Chem. Chem. Phys.* **12**, 12544–12555 (2010).
39. Gómez-Marín, A. M. & Feliu, J. M. in *Encyclopedia of Interfacial Chemistry: Surface Science and Electrochemistry* Vol. 5.2 (ed. Wandelt, K.) 820–830 (Elsevier, 2018).
40. Marković, N. M., Gasteiger, H. A. & Ross, P. N. Jr. Oxygen reduction on platinum low-index single-crystal surfaces in sulfuric acid solution: rotating ring–Pt(*hkl*) disc studies. *J. Phys. Chem.* **99**, 3411–3415 (1995).
41. Wang, J. X., Markovic, N. M. & Adzic, R. R. Kinetic analysis of oxygen reduction on Pt(111) in acid solutions: intrinsic kinetic parameters and anion adsorption effects. *J. Phys. Chem. B* **108**, 4127–4133 (2004).
42. Nishikawa, H. et al. Effects of sulfate on the oxygen reduction reaction activity on stabilized Pt-skin/PtCo-alloy catalysts from 30 to 80 °C. *Langmuir* **34**, 13558–13564 (2018).
43. Persson, A. E., Schoeman, B. J., Sterte, J. & Otterstedt, J.-E. The synthesis of discrete colloidal particles of TPA-silicalite-1. *Zeolites* **14**, 557–567 (1994).
44. Tsapatsis, M., Lovallo, M., Okubo, T., Davis, M. E. & Sadakata, M. Characterization of zeolite L nanoclusters. *Chem. Mater.* **7**, 1734–1741 (1995).
45. Nobbmann, U. & Morfesis, A. Light scattering and nanoparticles. *Mater. Today* **12**, 52–54 (2009).
46. Sakai, K., Hirano, T. & Hosoda, M. Electromagnetically spinning sphere viscometer. *Appl. Phys. Express* **3**, 016602 (2010).
47. O'Reilly, J. E. Oxidation–reduction potential of the ferro–ferricyanide system in buffer solutions. *Biochim. Biophys. Acta* **292**, 509–515 (1973).

## Acknowledgements

This work was supported by a Multidisciplinary University Research Initiative, sponsored by the US Department of the Navy, Office of Naval Research, under grant no. N00014-20-1-2418 (D.G.N. and J.A.M.), Star-Friedman Challenge grant from Harvard University (D.G.N. and J.A.M.), and Labex ARCANE, CB $\mu$ H-EUR-GS and ANR-17-EURE-0003 from the Agence Nationale de la Recherche (C.C.). J.A.M. acknowledges support from the Arnold and Mabel Beckman Foundation through a Beckman Young Investigator Grant. Part of this work was performed at the Center for Nanoscale Systems (CNS), a member of the National Nanotechnology Coordinated Infrastructure Network (NNCI), which is supported by the National Science Foundation under NSF award no. 1541959. A.E.T. acknowledges the Harvard University Center for the Environment for a postdoctoral fellowship, and D.P.E. acknowledges support from a DoD National

Defense Science and Engineering (NDSEG) fellowship. We thank B. Johnston, J. Cho and J. Shen for experimental assistance and M. J. Nava, J. Ryu, M. I. Gonzalez and Z. Yan for helpful discussions. We also thank G. M. Whitesides and M. S. Kodaimati for lending us a mass flow controller for the electrochemical experiments.

## Author contributions

A.E.T., D.P.E., D.G.N. and J.A.M. conceived the project. D.P.E. and J.A.M. designed the zeolite materials, and D.P.E. carried out the synthesis. A.E.T., D.G.N., C.C. and J.A.M. designed electrochemical experiments, and A.E.T. performed the electrochemical experiments. A.E.T. and D.P.E. performed testing and characterizations. C.C. performed electrokinetics modelling. All authors contributed to the manuscript preparation.

## Competing interests

D.P.E. and J.A.M. are inventors on a patent application related to O<sub>2</sub> concentration in microporous aqueous solutions held and submitted by Harvard University (application number PCT/US21/54267). The other authors declare no competing interests.

## Additional information

**Supplementary information** The online version contains supplementary material available at <https://doi.org/10.1038/s41929-023-00958-9>.

**Correspondence and requests for materials** should be addressed to Cyrille Costentin, Jarad A. Mason or Daniel G. Nocera.

**Peer review information** *Nature Catalysis* thanks Christopher Batchelor-McAuley, Serhiy Cherevko and the other, anonymous, reviewer for their contribution to the peer review of this work.

**Reprints and permissions information** is available at [www.nature.com/reprints](http://www.nature.com/reprints).

**Publisher's note** Springer Nature remains neutral with regard to jurisdictional claims in published maps and institutional affiliations.

Springer Nature or its licensor (e.g. a society or other partner) holds exclusive rights to this article under a publishing agreement with the author(s) or other rightsholder(s); author self-archiving of the accepted manuscript version of this article is solely governed by the terms of such publishing agreement and applicable law.

© The Author(s), under exclusive licence to Springer Nature Limited 2023